Supplement of Atmos. Chem. Phys., 22, 9175–9197, 2022
https://doi.org/10.5194/acp-22-9175-2022-supplement

Atmospheric Chemistry and Physics
Open Access

Supplement of

A novel pathway of atmospheric sulfate formation through carbonate radicals

Yangyang Liu et al.

Correspondence to: Liwu Zhang (zhanglw@fudan.edu.cn)

Table of Content

Supplementary Text Part A: Additional Details of Experimental Methods

S1 Measurements of sulfate yield on mineral dust proxies TiO_2+CaO as well as TiO_2+$CaCO_3$ upon irradiation.

30 mg of TiO_2+CaO and TiO_2+$CaCO_3$ mixtures after heat pretreatment were installed into the homemade quartz chamber. Afterward, a gas flow of (2.21×10^{14} molecules cm^{-3} SO_2/N_2+O_2 was introduced into the reaction chamber for 20 min under irradiation (RH = 30 % and Light intensity (I) = 30 mW cm^{-2}), and 25 mg of the particles were then taken out and dissolved into the 4 mL leaching solution (2 % vol. isopropanol), shaken by using an oscillator for 5 min, and the derived extracting solution was filtered with 0.22 μm PTFE membrane, followed by sending it into IC for sulfate ion measurements.

S2 Determination of reaction order.

Calculation of uptake coefficient is the way to describe the reaction efficiency of gas/surface interactions. Before that, sulfate formation rates as a function of SO_2 concentration were initially determined to verify its reaction order in the selected concentration range (400-20000 ppb), which is a crucial step to give a credible estimation of SO_2 uptake coefficient. Based on a prior study (Shang et al., 2010) with slight modification, SO_2 uptake on humidified particle surfaces depends on the SO_2 concentrations and reactive oxygen species (ROS), which thus could be described by the following equation (Eq. **S1**):

$$\frac{d[SO_4^{2-}]}{dt} = k[SO_2]^m[ROS]^l[H_2O]^n \quad \textbf{[S1]}$$

where $[SO_4^{2-}]$ refers to the sulfate production on humified particle surfaces, $[SO_2]$ to SO_2 gas concentration employed in the system, [ROS] to the concentration of active species produced on the particle surfaces, and $[H_2O]$ represents surface water concentration, and m, l, and n are the reaction orders of corresponding species. Assuming that [ROS] stays constant over the course of the experiment. Meanwhile, mass flow controllers provide stable gas flow and maintain the constant concentrations of humidified air, CO_2, and SO_2, which allow us to simplify the Eq. **S1** to Eq. **S2** through a logarithm function.

$$\lg\frac{d[SO_4^{2-}]}{dt} = \lg k + m\lg[SO_2] + C \quad \textbf{[S2]}$$

where C stands for Ilg[ROS] + nlg[H_2O], and $[SO_2]$ for the concentration of SO_2 where humidified particles are exposed. We then plotted the sulfate formation rate against exposed SO_2 concentration. Linear fitting analysis for those points resulted in the reaction order of 1.13 and 0.8 for the "TiO_2+CO_2+SO_2" and "TiO_2+$CaCO_3$+SO_2" reaction systems (Fig. S5). So far, 400 ppb is the lowest concentration that we are able to apply for the uptake measurements due to the limitation of the current experimental setup. While we note that the difference in SO_2 concentration between the lab and atmospheric conditions remains, employing hundreds of ppb SO_2 in the laboratory simulation to obtain the kinetic parameter of sulfate formation is acceptable (Liu and Abbatt, 2021; Liu et al., 2020). Taken above, we tentatively assume that uptake coefficients estimated under ppm level are valid, and those datasets derived from laboratory chambers are able to be generalized to the atmosphere condition.

S3 Measurements of sulfate yield on mineral dust proxies TiO_2 after exposure to SO_2 in the presence and absence of CO_2 upon irradiation.

25 mg of TiO_2 after heat pretreatment was installed into the homemade quartz chamber. Subsequently, particles were further pretreated under simulative solar irradiation for 1h with dry air gas flow (100 mL min^{-1}) to remove most of the carbonaceous residuals and impurities that remain on particle surfaces. Afterward, a gas flow of (7.37×10^{13} molecule cm^{-3} SO_2) /N_2+O_2 or (9.83×10^{15} molecule cm^{-3} CO_2) + (7.37×10^{13} molecule cm^{-3} SO_2) /N_2+O_2 were introduced into the reaction chamber for 3h under irradiation (RH= 30 % and Light intensity (I) = 30 mW cm^{-2}) and 15 mg of the particles were then taken out and dissolved into the 4 mL leaching solution (3 % vol. formaldehyde), shaken by using an oscillator for 5 min, and the derived extracting solution was filtered with 0.22 μm PTFE membrane, followed by sending it into IC for sulfate ion measurements.

S4 Gas sources and configuration set-up.

All gases used for experiments were purchased from Shanghai TOMOE gases CO., LTD. SO_2 (a mixture of 2.46×10^{15} molecule cm^{-3} SO_2 and balance gas N_2), CO_2 (a mixture of 2.46×10^{17} molecule cm^{-3} and balance gas N_2 or pure CO_2), and air with ultra-high purity of 99.999% were used as received. To precisely control the gas flow and concentrations, mass flow controllers (Beijing Sevenstar Electronics Co., Ltd.) was employed to adjust SO_2 or CO_2+SO_2 flows to the required concentration. With regard to the relative humidity (RH) adjustment, one pure dry air (21% O_2 and 79 % N_2) flow was humidified in a bubbler loaded with ultrapure water (electrical resistivity=18.2 MΩ). Together with rest gas flow equipped with MCFs, mixed gas with desired RH could be achieved. However, it should be noted that gas flow should be mixed for at least 1 h to reach a stable status prior to entrance into diffuse reflectance Fourier transformed

infrared spectroscopy (DRIFTS) or a homemade quartz chamber (d= 5.5 cm, H=1.2 cm, and actual volume = 20 cm^3).

S5 Mineral dust pretreatment and characterizations.

TiO_2 (Degussa P25) and $CaCO_3$ (Aladdin industrial Co., LTD) were used as reference dust particles in all tests. A pretreatment process was performed to remove the organic impurities and inorganic impurities such as bicarbonate and carbonate at TiO_2 and $CaCO_3$ surfaces using a thermal heating method in a tube furnace with the protection gas flow (dry air, 100 mL min^{-1}). Similarly, SiO_2 and Al_2O_3 (Aladdin industrial Co., LTD) went through the heat pretreatment described above (500 ˚C for 3 h). Mixtures of SiO_2, Al_2O_3, $CaCO_3$, and TiO_2 were prepared by manually grinding in the agate mortar. The crystalline phase of TiO_2 dust powder was analyzed by diffractometer with a Cu-Ka source. In addition, Brunauer-Emmet-Teller (BET) adsorption isotherm measurements were as well conducted using a Microm-eritics Asap 2000 surface area analyzer. The crystal structure of mineral dust proxy TiO_2 was characterized by Raman spectra (Jobin Yvon, Horiba Gr, France).

S6 *In situ* DRIFTS measurements.

To investigate the surface species during the heterogeneous reactions of SO_2 on mineral dust particles TiO_2, *in situ* DRIFTS (IRTracer-100, Shimadzu Instrument Corporation) analysis was conducted. Those FTIR spectra ranging from 4500 to 700 cm^{-1} were collected by using high-sensitivity mercury cadmium telluride (MCT) detector with a resolution of 4 cm^{-1} for 100 scans and recorded by a diffuse reflectance accessory. Thermocouple wires attached to the ceramic sample holder and a temperature controller were used, allowing resistive heating from simulated solar light (250 W xenon lamp, Beijing CEAULIGHT Co.Ltd., China) during the reaction. Moreover, a cooling circulation device was applied considering the temperature fluctuation of samples due to the long-term exposure to the light source. All measurements were carried out at 298 K. Prior to reaction gas entering the cell, further pretreatment was performed by sending dry airflow to the DRIFTS chamber under light irradiation for 1 h to remove the contamination residual on particle samples.

S7 IC measurements.

Sulfate ions formed on dust particles during the reaction were investigated by IC using a Metrohm 883 Basic IC system equipped with a Metrosep A supply 5-250/4.0 analytical column and a conductivity detector. Sample particles after reaction were extracted by an oscillator. The leaching solution (3 % formaldehyde solution applied for "TiO_2+(CO_2)+SO_2" system and 2 % isopropanol that applied for "TiO_2+$CaCO_3$+SO_2" system were prepared using ultrapure water of 18.2 Ω). These solutions served as a preservative to avoid S(IV) oxidation during the extraction through a 0.22 μm PTFE membrane filter, followed by IC measurement. In this work, we employed a scrubber system with an eluent of 3.2 mM Na_2CO_3/1.0 mM $NaHCO_3$ for anion measurement at a flow rate of 0.7 mL min^{-1}.

S8 Raman spectra.

In this study, an XploRA confocal spectrometer (Jobin Yvon, Horiba Gr, France) was applied for investigating dust particles after reaction. The Raman scattering was excited by an external-cavity diode (532 nm) and coupled with a 50× Olympus microscope objective (Olympus, 0.50 Numerical Aperture). Raman signals were acquired by a charge-coupled device (CCD) camera operating at 220 K with 1200 lines per mm diffraction grating. Samples after reaction were monitored at the range of 100-2000 cm^{-1} with twice repeated scans and 5 s exposure time per spectrum to give an overall view of mineral dust proxy TiO_2.

S9 ESR measurements.

Electron spin resonance (ESR) spectrometry was performed on a JES-FA200 Spectrometer and formed radicals using DMPO spin trap were recorded at room temperature for all measurements. The g factor in each data was calibrated using manganese standards. ESR spectrums were recorded after irradiation with a 500 W high-pressure mercury lamp (USH-500SC) for 2 min. The computer simulations of ESR spectrums were further conducted with the software Isotropic Radicals (Hagen, 2009) to identify active intermediates during the reaction course. For details, computer simulation of the four-line DMPO/·OH and six-line DMPO/SO_3^{-} radical adduct were obtained by setting the splitting constant of $a^N = a_\beta^H$; = 15.2 G, and a^N=14.7 G and a_β^H=16.05 G, respectively. Those employed constants compare favorably with the prior literature (Mottley and Mason, 1988).

S10 NTAS Measurements.

We utilized a nanosecond transient absorption spectroscopy (NTAS), designed and made by Dalian Institute of Chemical Physics, to investigate the possible heterogeneous reaction channels of sulfate formation on dust particles in the presence and absence of carbonate ions. About 35 mJ of the Nd: YAG laser source (355 nm, laser pulse 9 ns) entered into suprasil self-masking cuvettes (1 cm optical path and actual volume = 4 mL). All transient absorption spectra averaged by 10 times parallel results were obtained at room temperature. In addition, a monochromator and a photomultiplier tube with

a detection wavelength range from 200 to 800 nm enable us to monitor the considered active intermediates in the humidified mineral dust system. To visualize the signal of carbonate radical, we here applied single exponential decay curves (Eq. **S3,** the left side of the forward slash) to fit the signal of $CO_3^{\cdot-}$ evolved from TiO_2 suspension containing carbonate ions. The consumption process of carbonate radicals in chain reactions is described by a single exponential growth curve (Eq. **S3,** the right side of the forward slash).

$$y=a+be^{-\frac{x}{\tau}}/y=A+Be^{\frac{x}{\tau}} \quad [\mathbf{S3}]$$

where τ is the lifetime of carbonate radicals in each system. Constant functions were employed to fit the samples without NTA signals.

S11 Methodology for DFT calculations.

All electronic calculations were performed using Gaussian 09 program (M. J. Frisch, 2009). In recent years, numerous benchmarks concerning the performance of different Density Functional Theory (DFT) methods have proved that M06-2X functional is a reasonable choice for computing thermochemistry and barrier of atmospheric relevant systems (Elm et al., 2012; Mardirossian and Head-Gordon, 2016; Pereira et al., 2017; Zhao and Truhlar, 2008). Hence, geometry optimization of all the investigated species, including reactants, products, and transition states, and frequency calculations have been performed using the M062X functional coupled with the 6-311++G(3df, 3pd) basis set. Single point energy was calculated at CCSD(T)-F12/cc-PVDZ-F12 level of theory by ORCA 4.10 program using the geometry optimized at M06-2X/6-311++G(3df, 3pd) level (Knizia et al., 2009; Lane and Kjaergaard, 2009; Neese, 2012; Peterson et al., 2008; Yousaf and Peterson, 2008). In order to mimic the implicit solvent environment (Marenich et al., 2009), the solvation effect was introduced through the continuum solvation model based on solute electron density (SMD). The free energy in the solution was obtained using Eq. **S4**:

$$G^0 = E_0^{\text{CCSD(T)-F12}} + G_{\text{corr}}^{\text{M06-2X}} + \Delta G_{\text{SMD}}^{\text{M06-2X}} + \Delta G_{1\text{atm}\rightarrow 1\text{M}} \quad \textbf{[S4]}$$

$E_0^{\text{CCSD(T)-F12}}$ is the electronic energy obtained at the CCSD(T)-F12/cc-PVDZ-F12 level, $G_{\text{corr}}^{\text{M06-2X}}$ is the thermal correction to Gibbs free energy at the M06-2X/6-311++G(3df, 3pd) level under standard conditions (T=298K, P=1 atm), $\mathbf{\Delta}G_{\text{SMD}}^{\text{M06-2X}}$is the solvation free energy obtained from single point calculation at the M06-2X/6-311++G (3df, 3pd) level and $\mathbf{\Delta}G_{1\text{atm}\rightarrow 1\text{M}}$ is an additional term for converting the standard pressure of 1 atm in the gas phase to the standard concentration of 1 mol L^{-1} in solution (1.89 kcal mol^{-1}) (Marenich et al., 2009).

In the present system, one of the viable mechanisms to describe the reaction process is the hydrogen atom transfer (HAT) reaction. In this kind of reaction, transition states are necessary for calculating the activation free energy barrier term in HAT reaction. k_{act}, the thermal rate constant determined by activation free energy barrier, was calculated using the conventional Transition State Theory (TST)(Evans and Polanyi, 1935; Eyring, 1935; Truhlar et al., 1983) as implemented in 1 M standard state (Eq. **S5**):

$$k_{act}=l\kappa(T)\frac{k_BT}{h}\exp(\frac{-\Delta G^{\neq}}{RT}) \quad \textbf{[S5]}$$

Where l is the reaction path degeneracy accounting for the number of equivalent reaction paths. $\kappa(T)$, a temperature-dependent factor, corresponds to quantum mechanical tunneling and is approximated by Eq. **S6** according to Wigner (Elm et al., 2013; Wigner, 1932) for the HAT reaction; k_B is Boltzmann's constant, h is Plank's constant, and R is gas constant.

$$\kappa(T)=1+\frac{1}{24}(\frac{h\nu^{\mu}}{k_BT})^2 \quad \textbf{[S6]}$$

However, for a single electron transfer (SET) reaction, the transition state cannot be located using electronic structure methods, as it is not possible to describe the mechanistic pathway of electron motion. To estimate the reaction activation free energy barrier ($\Delta G^{\neq}$term), in such cases, the Marcus theory was used (Marcus, 1997). Within this transition-state formalism, the SET reaction activation free energy barrier ($\Delta G^{\neq}_{\text{SET}}$) is defined in terms of the difference of the Gibbs free energy between reactants and the products ($\Delta G^{0}_{\text{SET}}$) in SET reaction and the nuclear reorganization energy (λ) as follows (Eq. **S7**)

$$\Delta G^{\neq}_{\text{SET}}=\frac{(\lambda+\Delta G^{0}_{\text{SET}})^2}{4\lambda} \quad \textbf{[S7]}$$

While for λ, a very simple approximation was used as Eq. **S8**:

$$\lambda = \Delta E - \Delta G^{0}_{\mathrm{SET}} \quad \textbf{[S8]}$$

Where $\mathbf{\Delta}E$ is the non-adiabatic energy difference between reactants and vertical products.

It is expected that the tunneling effect would not be large for the reactions with low barriers (Iuga et al., 2015; Luo et al., 2017). Therefore, the tunneling effect was neglected in this SET reaction for its low barriers which will be discussed in detail in the R&D Section. In addition, diffusion should be considered especially for the low barrier SET reaction with k_{act} approximated to the diffusion limit (Luo et al., 2017). Thus, the Collins-Kimball theory(Kimball, 1949) was used to calculate the total rate constant k_{SET} or k_{HAT} which can be expressed as Eq. **S9**:

$$k_{\mathrm{SET}}(k_{\mathrm{HAT}}) = \frac{k_D k_{act}}{k_D + k_{act}} \quad \textbf{[S9]}$$

Where k_D is the steady-state Smoluchowski rate constant (Smoluchowski, 1917) for an irreversible bi-molecular diffusion-controlled reaction. Smoluchowski (Raymond, 2000) developed an empirical equation to calculate diffusion-controlled reaction rate constant k_D in an aqueous solution (Eq. **S10**):

$$k_D = \frac{2N_A k_B T (r_1 + r_2)^2}{3\eta r_1 r_2} \quad \textbf{[S10]}$$

Where N_{A} is the Avogadro constant, k_B is Boltzmann constant, T is temperature, η is the viscosity of water, and r_1, r_2 are the radius of the bi-molecular reactants.

S12 The procedures for oxygen isotope experiments.

Oxygen isotope experiments were divided into two parts: 1. preparation of $C^{18}O_2/N_2$ (2.46×10^{17} molecule cm^{-3}) through $C^{16}O_2$ exchanging with $H_2{}^{18}O$, 2. monitoring formed species using *in situ* DRIFTS. In the first step, a chamber was washed with ultrapure water (electrical resistivity= 18.2 MΩ), followed by drying the chamber using dry ultrapure N_2 gas flow (300 mL min^{-1}, 40 min). Afterward, we introduced $H_2{}^{16(18)}O$ into the chamber with a pipette and operated this process in the glove box with N_2 atmosphere, where contents of H_2O were rigorously controlled below 2.46×10^{13} molecule cm^{-3} to prevent the undesired exchange of ^{18}O with ^{16}O in the atmosphere. In the next step, we extracted the gas from the chamber and added it with CO_2 for O exchange (70 min). For these two sets of DRIFTS studies, TiO_2 particles went through in situ heat pretreatments in the sample holder with an airflow (150 mL min^{-1}) at 500°C for 0.5 h. Subsequently, TiO_2 particles were cooled down to room temperature using a cooling device attached to the DRIFTS for 35 min. Afterward, the chamber was sealed with gas-tight sample pads and we evacuated the chamber, followed by introducing $C^{16(18)}O_2/N_2$. After adsorption of CO_2/N_2 for 20 min, TiO_2 was exposed to 6.14×10^{15} molecule cm^{-3} of SO_2/N_2+O_2 (RH= 30 %) for 60 min and we monitored the sulfate formation under irradiation (light intensity (I) = 30 mW cm^{-2}) for each set of experiment.

S13 Chemical analyses.

Water-soluble ions in the atmospheric particulate matter were measured using a Metrohm 883 Basic IC system, which is equipped with a Metrosep A Supply A-250/4.0 anion analytical column or a C-150/4.0 cation analytical column and a conductivity detector; eluent: 3.2 mM Na_2CO_3/1.0 mM $NaHCO_3$ for anion measurements at a flow rate of 0.7 mL min^{-1}; 1.7 mmol L^{-1} HNO_3 for cation measurements at a flow rate of 0.9 mL min^{-1}; inject volume: 20 uL. A series of Li^+, NH_4^+, Ca^{2+}, Mg^{2+}, Na^+, K^+, F^-, CH_3COO^-, $COOH^-$, Cl^-, NO_2^-, NO_3^-, PO_4^{3-}, SO_4^{2-}, and $C_2O_4^{2-}$ ions were analyzed. Each collected filter membrane was cut and placed into a 50 mL PET vial, followed by ultrasonically extracting for 40 min with 20 mL ultrapure water (R ≥ 18.0 MΩ). For each sample, we applied two PTFE filter chips to remove insoluble particulate matter before being sent into IC. Obtained ion concentrations were further transformed to the data in the unit of μg m^{-3} on the basis of Eq. **S11**:

$$\rho = \frac{(\rho_1 - \rho_0) \times V \times N \times D}{V_{nd}} \quad \textbf{[S11]}$$

where ρ represents the ions concentration (μg m^{-3}), ρ_1 is the measured ions concentration of membrane after sampling (mg L^{-1}), ρ_0 is the measured ions concentration of membrane before sampling (mg L^{-1}), V is the volume of extracting solution for sample (L), and N refers to divisions for membrane, D to the dilution coefficient, and V_{nd} to the total sampling volume.

Supplementary Text Part B: Additional Discussion on Data

S14 Characterization of mineral dust proxies TiO_2 and $CaCO_3$.

To examine how relevant are the physicochemical properties of employed mineral dust proxies in this work to those reported in the early studies and to provide convincible results shown in this work, characterization of mineral dust proxies was conducted. Commercial TiO_2 (Degussa P25) and $CaCO_3$ particles (Shanghai Aladdin Chemical Reagent Co.) after heat pretreatment and grinding process were initially characterized by X-ray diffraction and N_2 adsorption-desorption isotherm. Measurement results confirm the coexistence of the anatase phase and rutile phase in TiO_2 (Qin et al., 2009) as well as monoclinic $CaCO_3$ (Chen et al., 2022) (Fig. S1A), with the surface area of 56.44 m^2 g^{-1} and 1.25 m^2 g^{-1} determined for ground TiO_2 and $CaCO_3$, respectively, consistent with early observations in the literature (Di Fonzo et al., 2009) (Johnson et al., 2005).TiO_2 and $CaCO_3$ particles after heat pretreatment, weighted in identical mass, were ground in an agate mortar for 10 min to obtain TiO_2 (50 wt. %) + $CaCO_3$ (50 wt. %) particles. The XRD pattern of TiO_2 (50 wt. %) + $CaCO_3$ (50 wt. %) shows the feature assembly of XRD patterns of ground TiO_2 and $CaCO_3$ particles, with surface area determined to be 23.52 m^2 g^{-1}, slightly lower than the averaged surface area of TiO_2 and $CaCO_3$ particles. In Fig. S1B, anatase crystal with tetragonal structure and rutile crystal of P4/mnm space group were further probed by Raman spectra, with several active optical phonon modes at the vicinity of 141, 192, 392, 512, and 632 cm^{-1}, which are in good agreement with previous studies (Balachandran and Eror, 1982; Su et al., 2008). Overall, the above measurements allow us to deduce the physicochemical properties of mineral dust proxies applied in this study agree with those reported in the early works.

S15 Comparison between CaO and $CaCO_3$ particles regarding physical properties (BET surface area, surface PH, hygroscopicity as well as solubility).

In our main text, our quantification analysis results (Fig. 2 and b) show that the presence of carbonate species is likely to increase sulfate production through a new pathway where carbonate species may play a different role in sulfate production beyond creating an alkaline environment. Especially, to rule out the possibility that the evident increase of sulfate production in $CaCO_3$+TiO_2 particles relative to CaO+TiO_2 particles upon irradiation relates to the intrinsic difference between $CaCO_3$ and CaO, i.e. the physical properties.

The CaO particles applied in our experiment are commercially available from the SINOPHARM company, and the BET surface area is determined to be 2.54 m^2 g^{-1} in the literature (Tang et al., 2016). On the other hand, the BET surface area for $CaCO_3$ particles in this study was determined to be 1.35 m^2 g^{-1} (Quantachrome). Hence, $CaCO_3$ particles disadvantage in BET surface area compared to CaO, and it would not be the factor that increases sulfate yield. Our early study measured the pH of leaching solution of 0.625 mg $CaCO_3$ + 0.625 mg TiO_2 and 0.625 mg CaO + 0.625 mg TiO_2, and they are 9.27 and 11.26, respectively (Fang et al., 2021). On this basis, we could deduce that the surface pH of CaO is higher than $CaCO_3$.

We also compared the hygroscopicity of $CaCO_3$ and CaO by specifying RHs that allow them to form a monolayer of water. A prior study shows that a monolayer of water formed on the surface of $CaCO_3$ particles when RH is over 52 % (Li et al., 2010). On the other hand, RH of 27 % enables CaO to form a monolayer of water (Goodman et al., 2001). While those results are collected from different literature and bias may come from different measurement systems. However, this evident gap leads us to conclude that CaO exhibits a stronger hygroscopicity than $CaCO_3$ does. Following this, we believe at least the hygroscopicity is not the force to produce more sulfate over TiO_2+$CaCO_3$ relative to TiO_2+CaO upon irradiation. Additionally, this comparison also gives an explanation for substantial sulfate production at the surface of TiO_2+CaO under illumination due to its strong hygroscopicity.

Solubility information is obtained from "CRC CHEMISTRY and PHYSICS HANDBOOK (97th Edition, 2016)", where calcium carbonate (calcite) is 6.6 mg/100 g H_2O (Section "Physical Constants of Inorganic Compounds", page 4-53). However, the specific solubility of CaO is not available in this handbook or literature we have been searching for so far. Nevertheless, CaO is likely to have a higher solubility than calcium carbonate since it can react with H_2O to form $Ca(OH)_2$ and form a saturated solution (160 mg/100 g H_2O) (Chrzan, 1987).

Collectively, we show that $CaCO_3$ shows humble physical properties including BET surface area, hygroscopicity as well as solubility relative to CaO while TiO_2+$CaCO_3$ particles have higher sulfate production than TiO_2+CaO particles do under irradiation. Together with the observation of sulfate production over TiO_2/$CaCO_3$/TiO_2+$CaCO_3$, in combination with the analysis of sulfur species over TiO_2+CaO/TiO_2+$CaCO_3$, active intermediates derived from TiO_2+$CaCO_3$ are speculated to account for the increased sulfate production

S16 Role of carbonate species in promoting sulfate production in the TiO_2+$CaCO_3$ mixture.

It remains a puzzle for the role of carbonate salt in sulfate formation either by favoring neutralization of H_2SO_4 on alkaline surfaces or by serving as the precursor of active CO_3^- to trigger the fast sulfate formation as we proposed in this work. According to the EDS mapping analysis of relevant component contents of the Arizona test dust (ATD) (Table 2), the mass fraction ratio of TiO_2 to $CaCO_3$/CaO is thus fixed at 1:7 to mimic the synergistic effect that is likely to take place over the authentic dust particles. In the dark experiments, both TiO_2+CaO and TiO_2+$CaCO_3$ almost yield an

identical concentration of sulfite and sulfate, indicating that they show similar surface properties, e.g. alkalinity and the number of surface sites. Once irradiated, the total sulfur content, i.e. S(IV)+S(VI), in TiO_2+$CaCO_3$ particles is quite higher than that in TiO_2+CaO particles upon irradiation, whereas they are almost identical in the dark experiments. Consequently, the difference between two mixtures regarding sulfate yield under illumination can be mainly attributed to the reaction pathway that has not been previously considered. Another plausible explanation is that carbonate radical ions promote sulfate formation in the gas phase due to the production of gas-phase carbonate radical ions.

S17 Inconsistency between our study and the reported results regarding the response of SO_2 oxidation to solar irradiation over Fe_2O_3 particles.

We are aware of the inconsistency between our study and the reported results in the literature (Li et al., 2019; Toledano and Henrich, 2001). Toledano et al. observed a UV-induced increase in adsorption of SO_2 over αFe_2O_3 (0001). The difference may correlate to the different light sources and dust sources. In our lab study, 30 mW cm^{-2} of photon flux was applied using a solar simulator, corresponding to 0.3 times of AM 1.5 G solar irradiance while they employed a focused 200 W Hg(Xe) lamp, which provides a strong light source, with $h\nu > E_{gap}$ (2.2 eV) roughly 70 times of the solar flux in that wavelength range. On the other hand, we adopted commercially available αFe_2O_3 nanoparticles and the chemical properties of which are believed to be different from that of single-crystal Fe_2O_3 with a pure (0001) surface. This is because the crystal plane, morphology, and size of semiconductor materials altogether determine the inherent band gaps (the position of the conduction band relative to the position of the valence band) of semiconductors (Alivisatos, 1996; Xu et al., 2013; Xu et al., 2015). In Li's work, they synthesized four types of Fe_2O_3 nanomaterials in different morphologies, which have a various abundance of crystal facets. This leads to distinct photochemical properties compared to pristine Fe_2O_3 nanoparticles.

In addition, we observed a slight decrease in sulfite and sulfate yield upon irradiation compared to dark experiments, consistent with Du's work (Du et al., 2019), in which a more evidently decrease was found in the initial reaction stage. A plausible explanation for this observation is that while we applied a xenon lamp as the light source for experiments, elevated temperature in the chamber is likely to decrease the SO_2 uptake over dust particles, more evidently for those particles with dark colors. This agrees with findings in our early study where SO_2 uptake over αFe_2O_3 particles is sensitive to temperature (Wang et al., 2018), and persistent increase in temperature hinders SO_2 adsorption and consequently reduces sulfate yield.

S18 Crystal type and phase of Ti-containing authentic mineral dust particles.

Considering that TiO_2 content is not necessarily an accurate predictor of photoreactivity, more information related to Ti species in these mineral dust particles would help us to understand the different promotional effects of CO_2 on sulfate production. Especially, only the anatase phase of TiO_2 is observable in Kaolin (K-Ga-2) through differential thermal analysis, chemical analysis shows that TiO_2 accounts for 2.08 % wt. of the total mass of K-Ga-2 (Johnson et al., 1982), consistent with early observation where anatase is general phase found in Kaolin clay (Weaver and Minerals, 1976). For Illite (IMt-2), TiO_2 is in rutile phase and accounts for 0.87 % wt. of total mass (Gailhanou et al., 2012). TiO_2 phases of anatase and rutile altogether account for Ti-containing components in Arizona test dust (ATD) particles (Joshi et al., 2017), where 0.3 % of TiO_2 is determined in the work of Joshi and coworkers and 0.5-1 % of TiO_2 is provided by the supplier. Anatase TiO_2 exhibits more efficient production of hydroxyl radicals than rutile TiO_2 in the presence of adsorbed hydroxyl groups and water layers (Buchalska et al., 2015), with more efficient production of carbonate radicals correspondingly. This gives an alternative explanation why in the presence of CO_2 under irradiation Kaolin (K-Ga-2) exhibits a more pronounced increase in sulfate production than Arizona test dust (ATD) and Illite (IMt-2).

S19 Experimental evidence of the production of $CO_3^{\cdot-}$ in the carbonate-salt containing TiO_2 suspension using probe molecular aniline.

To probe the formation of carbonate radical over carbonate-containing TiO_2 particles under irradiation, aniline is used as a probe molecular, which is reported to have a high reaction rate with carbonate radical ions ($k_{\cdot OH,\ aniline} = 6.5\times10^9$ $M^{-1}s^{-1}$) (Samuni et al., 2002). In Fig. 9, a difference between the "air+Irradiation" system and the "TiO_2+air+Irradiation" system mainly comes from the contribution of hydroxyl radical instead of from other intermediates (e.g. superoxide radical, see discussion in main text). When carbonate ions were introduced into TiO_2 suspension, leaving the pH of the reaction system at 11, the removal rate of aniline was evidently increased. We noted that increasing pH favors the formation rate of ·OH radical, which has been well verified in numerous works (Chavadej et al., 2008; Kansal et al., 2008; Tang and An, 1995). To examine the net contribution of carbonate radical ions to the increased oxidation capability of the carbonate-containing TiO_2 system beyond the increased pH environment, we performed the reference experiment using the "TiO_2+air+NaOH" reaction system. In detail, an adequate amount of NaOH was added to TiO_2 suspension to have the pH of TiO_2 suspension comparable to that of TiO_2+Na_2CO_3. Indeed, it shows a higher removal rate than"TiO_2+air" but a lower removal rate than"TiO_2+ Na_2CO_3+air". This result seems to suggest that alkaline carbonate salt favors promoting sulfate formation in part due to the increasing OH yield. Nevertheless, one should note that

carbonate radical ions are the predominant species in a relatively strong alkaline environment in the presence of carbonate since the (bi)carbonate ions are excellent ·OH scavengers.

S20 Theoretical studies of two reaction routes for producing carbonate radicals.

In the present system, one of the viable mechanisms for the formation of $CO_3^{\cdot-}$ is hydrogen atom transfer (HAT) reaction (**RS1**) through ·OH with HCO_3^-. Such optimized structures involved in the HAT process as a reactant (React), transition state for the reaction step (TS), and the resulting product (Prod) were displayed in Fig. S10A. In HAT reaction, HCO_3^- transfers a H atom to O atom in ·OH, leading to the formation of H_2O and $CO_3^{\cdot-}$. The corresponding calculated activation free energy barrier $\Delta G^{\neq}_{HAT}$ was 9.02 kcal mol^{-1}, which is low enough for the HAT reaction of ·OH and HCO_3^- to occur rapidly. The rate constant k_{HAT-1} predicted for the HAT reaction was 4.04×10^6 M^{-1}s^{-1}.

$$\cdot OH + HCO_3^- \xrightarrow{k_{HAT-1}} CO_3^{\cdot-} + H_2O \qquad \textbf{[RS1]}$$

In addition, the formation of $CO_3^{\cdot-}$could be also through the SET reaction (**RS2**) of ·OH with CO_3^{2-}. As shown in Fig. S10B, O atom in CO_3^{2-} transfers an electron to O atom in ·OH to form $CO_3^{\cdot-}$and OH^-. This SET reaction is thermodynamically favorable, with the difference of Gibbs free energy between reactant and product ΔG^0_{SET} lying at -9.74 kcal mol^{-1}. The corresponding calculated activation free energy barrier $\Delta G^0_{SET}$is 0.02 kcal mol^{-1}, which is low enough for this thermal process to be faster than that controlled by the diffusion. Thus, the SET process for ·OH and $CO_3^{2-}$is diffusion-controlled. The rate constant k_{SET-2} predicted for SET process between ·OH and CO_3^{2-} was 7.65×10^9 M^{-1}s^{-1}.

$$\cdot OH + CO_3^{2-} \xrightarrow{k_{SET-2}} CO_3^{\cdot-} + OH^- \qquad \textbf{[RS2]}$$

S21Estimation of oxygen consumption and supply flux.

When (bi)carbonate ions are introduced into the reaction, they serve the excellent ·OH scavenger to form $CO_3^{\cdot-}$, leaving two major active intermediates $O_2^{\cdot-}$ and $CO_3^{\cdot-}$ responsible for fast sulfate formation. Assuming that bi(carbonate) ions fully capture ·OH, in combination with the scavenger experiment results, the relative contribution of $CO_3^{\cdot-}$ and $O_2^{\cdot-}$ to overall sulfate formation over TiO_2 particles could be assumed to be 0.7 and 0.3, respectively. Together with the major SO_2 oxidation reaction channel considered above, one may note that 1 mole of oxygen contributes to 1.7 moles of sulfate, and H_2O provides an additional oxygen source compensating for the oxygen deficit. Given the measured SO_2 uptake coefficient in the DRIFTS chamber, the sulfate formation rates are thus determined to be 0.33 μM s^{-1} m^{-2} for the geo surface of TiO_2 particles, known as the upper limit of uptake capability, corresponding to the maximum oxygen consumption rate of nearly 0.19 μM s^{-1} m^{-2}. For TiO_2+$CaCO_3$ particles, the sulfate formation rate is 2.01 μM s^{-1} m^{-2}. We applied the above relation (1 mole of oxygen ~ 1.7 moles of sulfate) for calculating the oxygen consumption rate in the TiO_2+$CaCO_3$ system. This operation will lead to a conservative estimation of oxygen consumption rate since the relative contribution of carbonate radical ions to sulfate formation are expected to be even more predominant in the "TiO_2+$CaCO_3$+air" system (1 mole of oxygen ~ 2 moles of sulfate) than that in "TiO_2+CO_2+Air" system (1 mole of oxygen ~ 1 mole of sulfate). Therefore, the oxygen consumption rate is not likely to exceed 1.18 μM s^{-1} m^{-2}

We further considered the oxygen supply capability over water layers attached to the dust particles. A steady-state of gas diffusion is described as a state where the diffusion flux density J_s, stays constant and by integration from 0 to l. Fick's first law can be expressed in the following form **RS3** (Nguyen et al., 1992):

$$J_s = -D\frac{\Delta C}{l} \qquad \textbf{[RS3]}$$

where, ΔC is the concentration difference between saturation and the system at a given time, D the mass transfer coefficient (0.021 millimeters^2 s^{-1}), and l the distance between water layers with gradient oxygen concentration. At RH of 30 %, nearly two aqueous-like water layers are speculated to absorb onto the dust particle surface (Mogili et al., 2006) (Peters and Ewing, 1997), and around 0.3 nm, known as the typical thickness feature for mono water layer (Ali et al., 2015; Gao et al., 2020; Ruiz-Agudo et al., 2013), and 0.6 nm was thus adopted for l. For a degassed single water layer devoid of O_2 in our system, the flux of O_2 supplied across the two aqueous-like water layers is at a rate of 17.08 M s^{-1} m^{-2}, which is several orders of magnitude higher than that of oxygen consumption determined for both "TiO_2+CO_2+Air" and "TiO_2+$CaCO_3$" systems. Therefore, oxygen is sufficient in the reaction, allowing the considered chain reactions to continually proceed.

S22 Definition and determination of equivalent exposure time.

Following Jiang's work (Jiang et al., 2019), we introduce the concept of "equivalent exposure time" in analyzing the DRIFTS data. The "equivalent exposure time" refers to the theoretical exposure time of SO_2 at an atmospherically-relevant concentration that TiO_2 and TiO_2+$CaCO_3$ particles are exposed to. The equivalent exposure time is calculated

by multiplying the reaction time applied in the lab with the scale factor, which is the ratio of SO_2 concentration applied in DRIFTS experiments to SO_2 concentration monitored in the atmospherically-relevant condition (20 ppb, assumed). Nevertheless, considering a large SO_2 concentration gap between the lab simulations and field observations, direct extrapolation of equivalent exposure time into such low SO_2 concentration may not be appropriate. Therefore, the reaction kinetics of SO_2 on mineral dust particles of concern was investigated, and it is evidenced to follow the pseudo-first-order in the SO_2 concentration range of 400-20000 ppb (Fig. S5), which cover all SO_2 concentration applied in this study. While a concentration gap between lab studies and field observation remains, we tentatively assume this gap slightly impacts the kinetics considered. On this basis, we plotted integrated areas for sulfate species versus equivalent exposure time (Fig. S12).

S23 Observation of suppressed sulfate production in "SiO_2+H_2O_2+SO_2+CO_2" reaction system.

SiO_2 particles are the most dominant constituent of mineral dust particles ($\geq$ 60 %) (Ji et al., 2015). We supplied the data showing that CO_2 of atmospherically relevant concentration decreases the sulfate production over SiO_2 particles in the presence of gaseous H_2O_2 (Fig. S15). H_2O_2 is introduced into the reaction system as SiO_2 has rather lower SO_2 uptake coefficients ($<1\times10^{-7}$) than other crust constituents, e.g. (α-$Al_2O_3\approx1.6\times10^{-4}$ and α-$Fe_2O_3\approx7.0\times10^{-5}$) (Crowley et al., 2010; Usher et al., 2002). The difference in sulfate production in two reaction systems ("SiO_2+SO_2" and "SiO_2+CO_2+SO_2") can not be easily observed otherwise.

Table S1. Estimation for Sulfate Formation Rate and Uptake Coefficient of SO_2.

	Carbonate Fraction (wt. %) / CO_2 Concentration ($\times 10^{15}$ molecule cm^{-3})	Sulfate Formation Rate ($\times 10^{12}$ ion s^{-1})	Uptake Coefficient ($\times 10^{-5}$)
TiO_2+$CaCO_3$+SO_2	0	2.55 ± 0.04	1.17 ± 0.02 *
	50	45.76 ± 0.56	20.89 ± 0.24
	100	2.68 ± 0.32	1.23 ± 0.15
TiO_2+CO_2+SO_2	0	2.37 ± 0.16	2.23 ± 0.02 *
	4.91	3.03 ± 0.27	2.80 ± 0.25
	9.83	3.59 ± 0.49	3.38 ± 0.05

*It is notable that difference would take place with regard to the uptake coefficients of pristine TiO_2 in the "TiO_2+($CaCO_3$)+SO_2" and "TiO_2+(CO_2)+SO_2" systems. This is mainly due to the different reaction conditions and varied approaches for uptake estimations in these two systems.

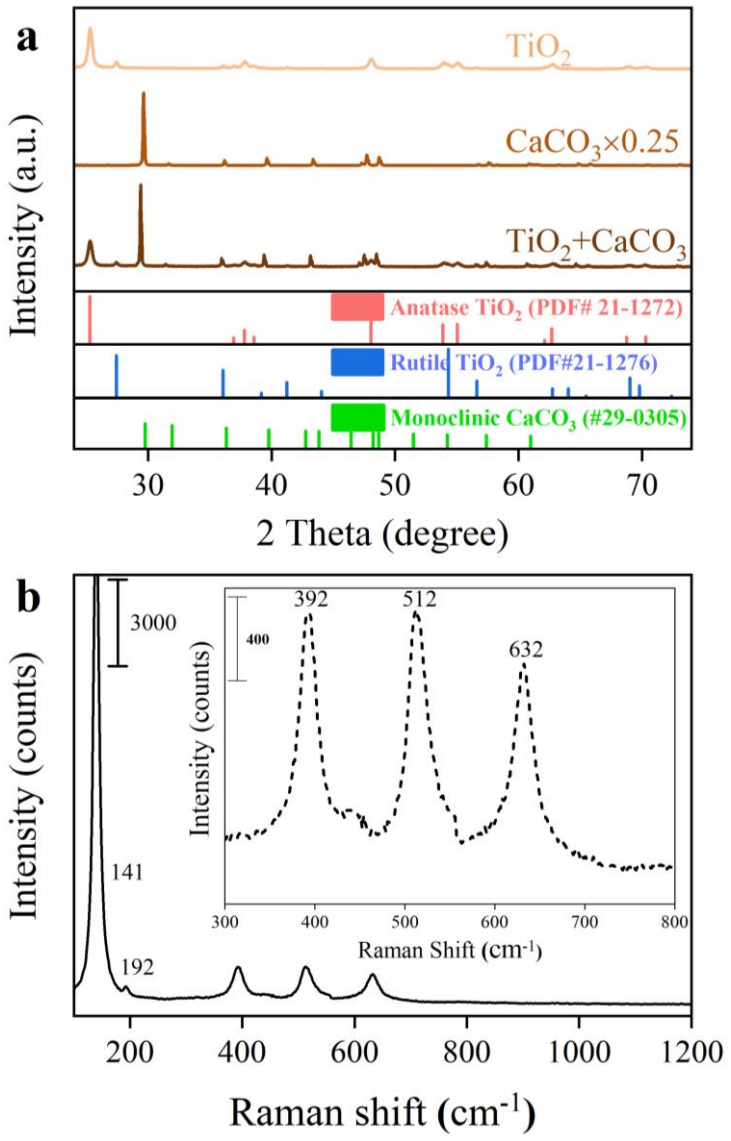

Fig. S1. Characterizations of mineral dust particles. (**a**) XRD patterns of TiO_2, $CaCO_3$ as well as TiO_2 (50 % wt.)+$CaCO_3$ (50 % wt.) particles, respectively. (**b**) Raman spectra of TiO_2 particles. Standard PDF cards for anatase and rutile phases of TiO_2, as well as monoclinic $CaCO_3$, were compared as a reference.

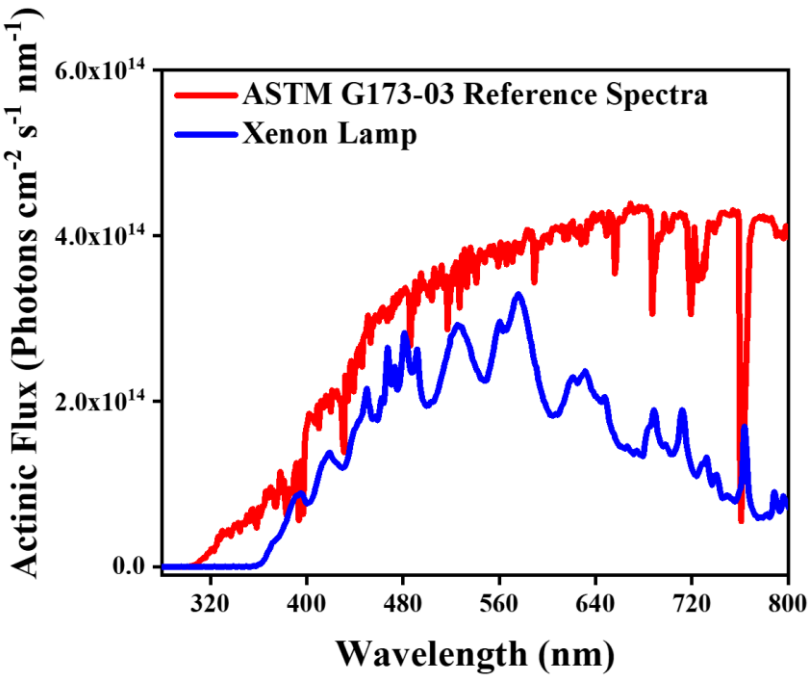

Fig. S2. The actinic flux of solar irradiance spectra ASTM G173-03 and a xenon lamp. ASTM G173-03 refers to the "Standard Tables for Reference Solar Spectral Irradiances: Direct Normal and Hemispherical on 37deg; Tilted Surface", which served as a reference spectra for comparison.

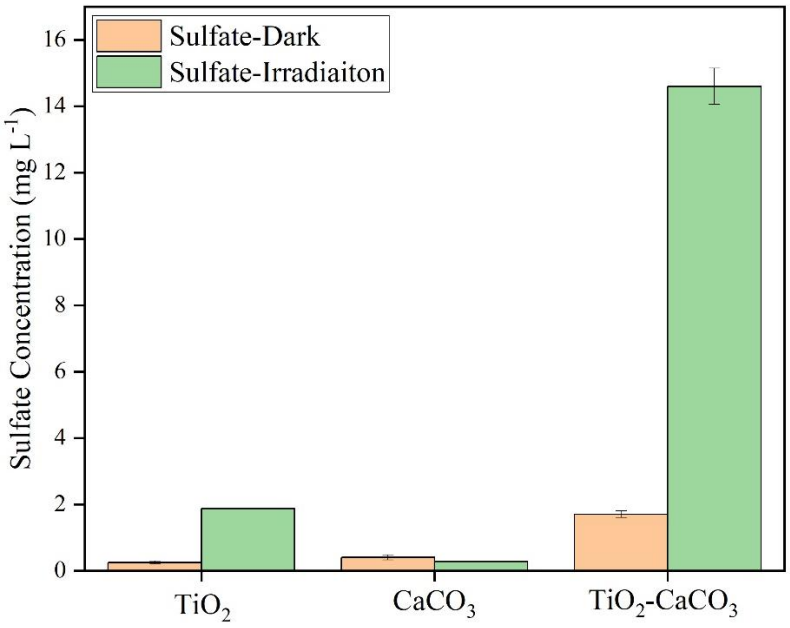

Fig. S3. Sulfate concentration quantified by IC on mineral dust particles after exposure to gaseous SO_2 under dark or irradiation for 60 min. Reaction conditions: RH = 30 %, Light intensity (I) = 30 mW cm^{-2}, Total flow rate = 52.5 mL min^{-1} and $SO_2 = 2.21\times10^{14}$ molecules cm^{-3}.

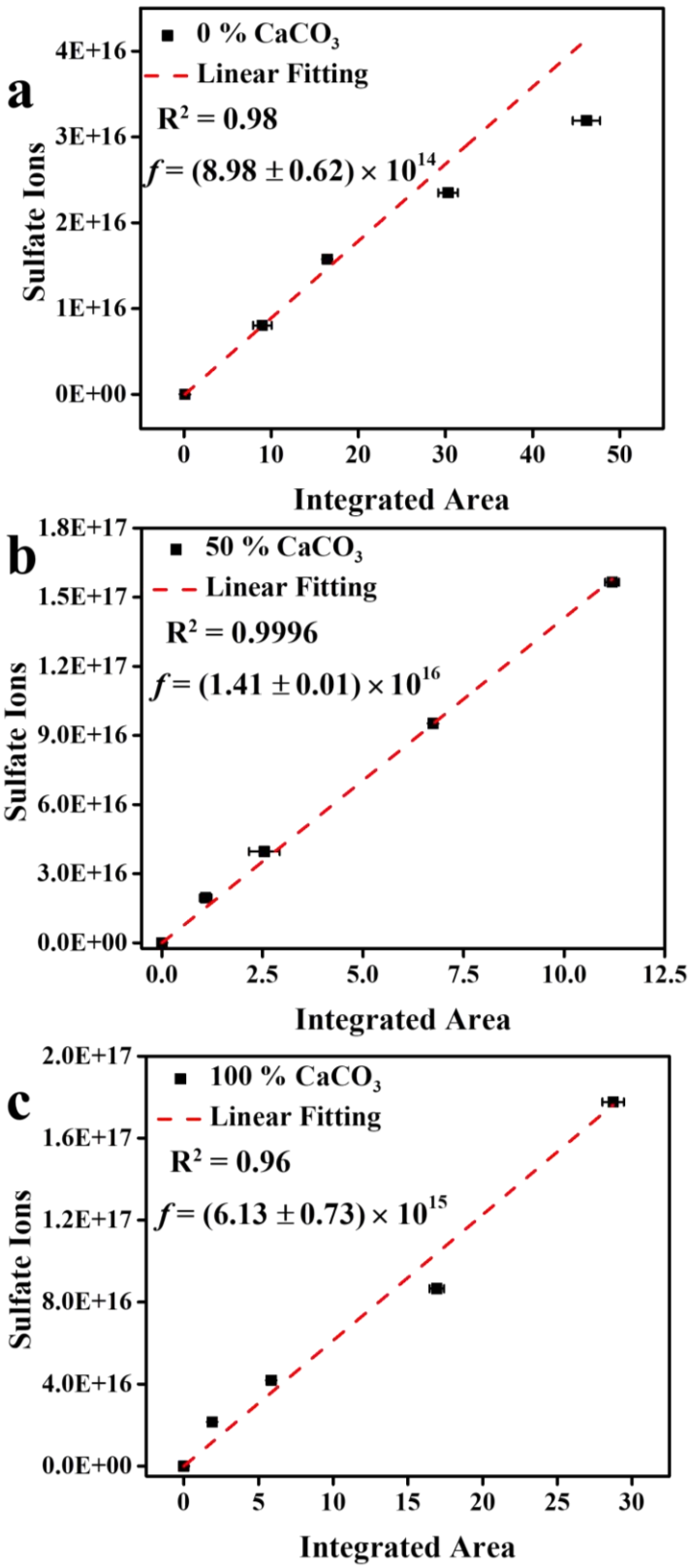

Fig. S4. Calculation of the conversion factor for each type of particle of interest. The infrared absorption calibration curves were obtained using known proportions of K_2SO_4 and dust particles (**a**) TiO_2, (**b**) TiO_2 (50 wt. %) + $CaCO_3$ (50 wt. %), and (**c**) $CaCO_3$, respectively. Uncertainties on conversion factors represent the standard deviation of the slopes obtained from the linear regression analysis.

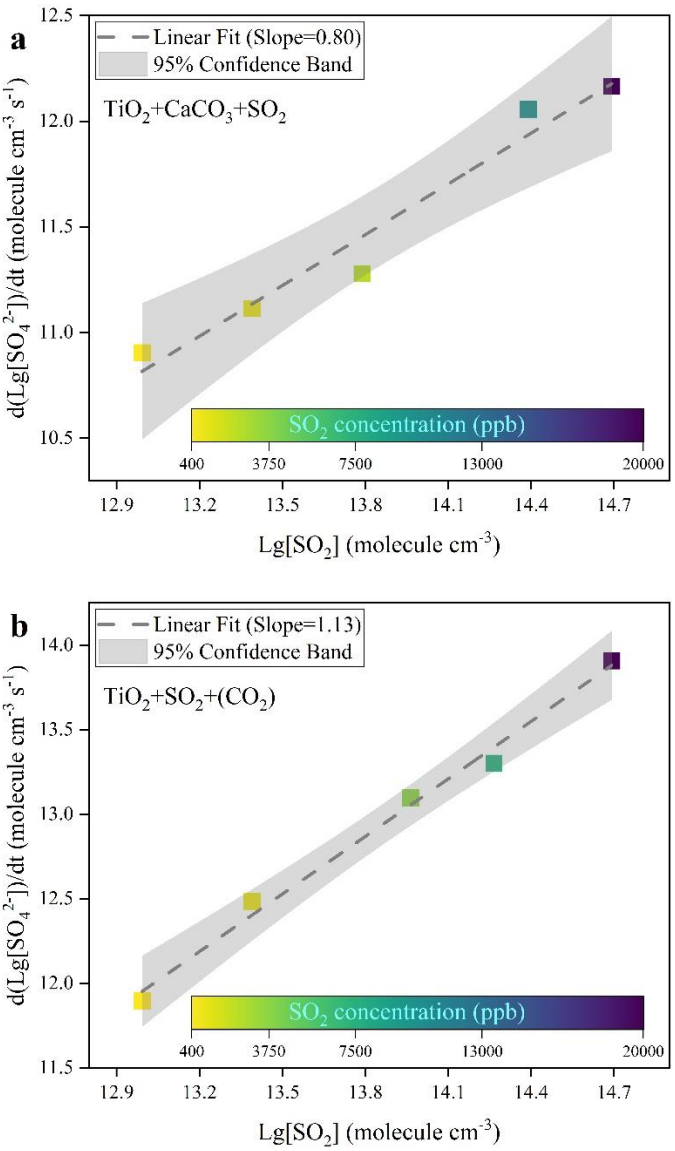

Fig. S5. Reaction order determination. The Lg-Lg curve of the sulfate production rate of TiO_2 **(a)** in the presence of CO_2 (400 ppm) and **(b)** mixed with $CaCO_3$ (50 wt. %) upon varied SO_2 concentration exposure (400-20000 ppb, RH= 30 %) under irradiation (30 mW cm^{-2}) plotted against the concentrations of SO_2 molecules exposed.

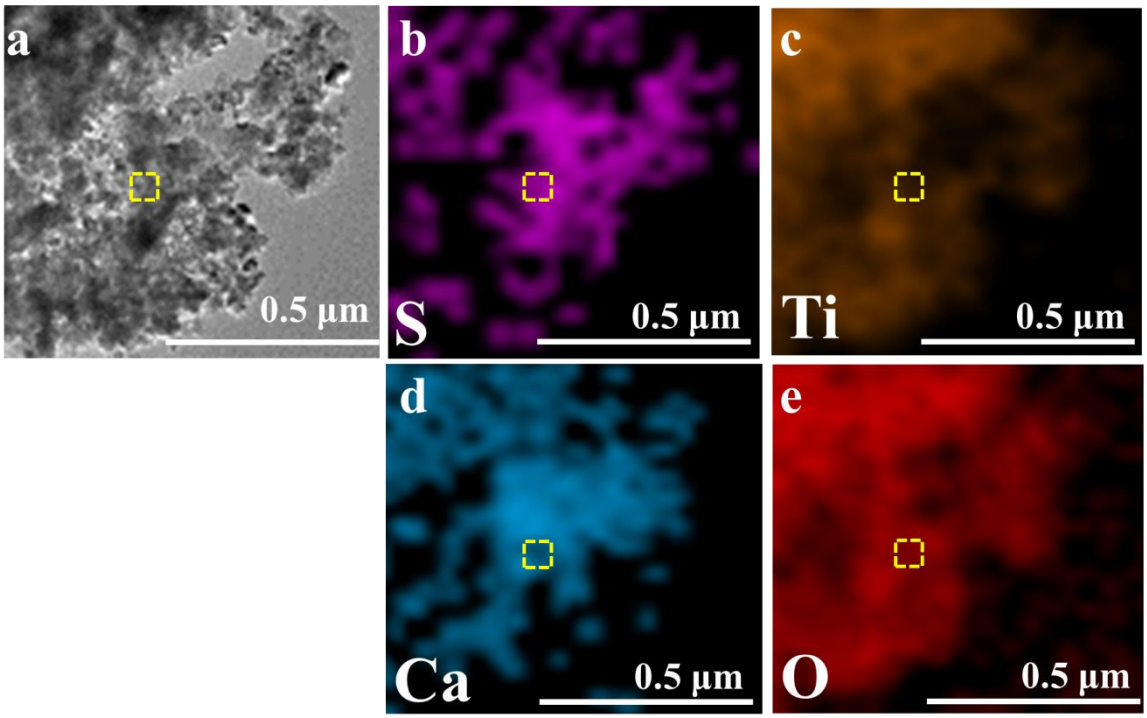

Fig. S6. The HRTEM image: (**a**) and element mappings (**b-e**) for dust particles after reaction. TiO_2 (50 wt. %)+$CaCO_3$ (50 wt. %) particles after being exposed to the SO_2/N_2+O_2 gas flow for 60 min. Reaction condition: $[SO_2] = 4.4\times10^{14}$ molecule cm^{-3}, RH= 30 % and Irradiation intensity = 30 mW cm^{-2}.

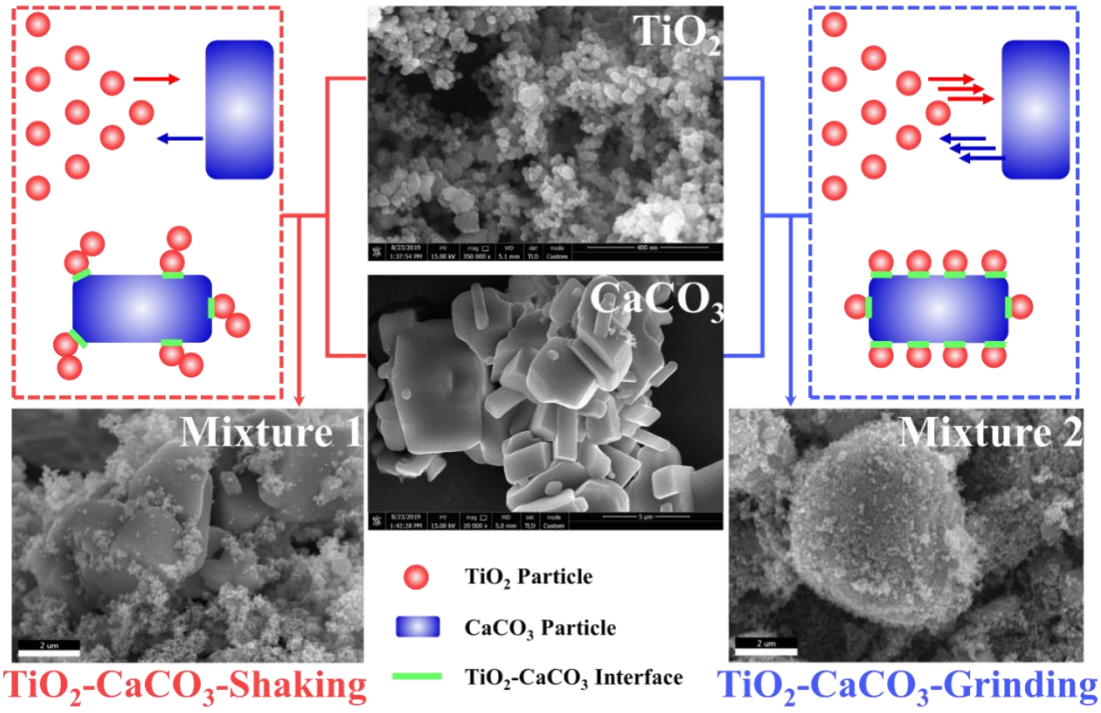

Fig. S7. Scanning electron microscope (SEM) of particles of interest. Noting that the mixture 1 and 2 refer to the particles composed of 50 % mass fraction of TiO_2 and 50 % mass fraction of $CaCO_3$ prepared through the manually-shaking method and manually-grinding method, respectively.

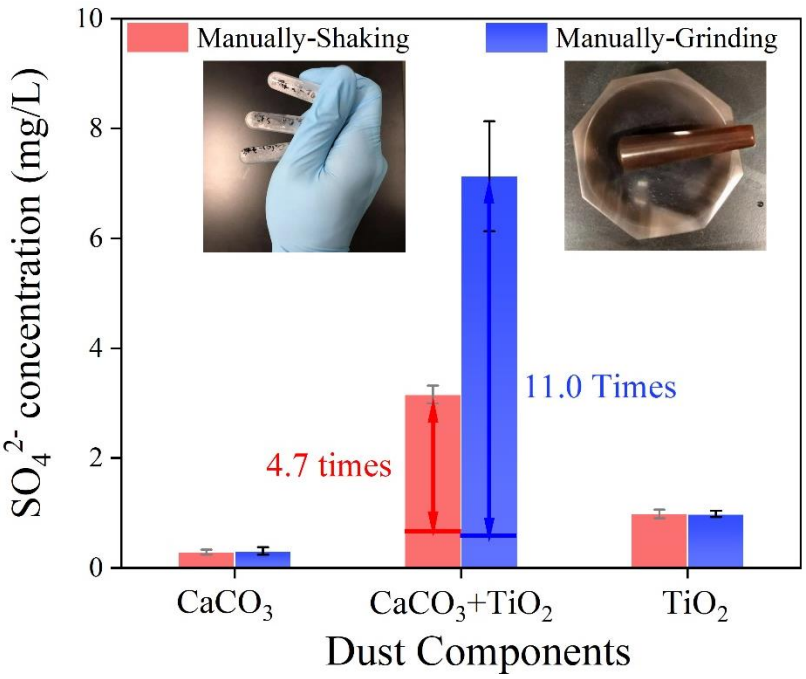

Fig. S8. The heterogeneous reaction of SO_2 on mineral dust surfaces in two TiO_2 (50 wt. %)+$CaCO_3$ (50 wt. %) systems. Sulfate concentration measured by IC on mineral dust surfaces after exposure to gaseous SO_2 under irradiation. Reaction condition: SO_2 concentration = 2.21×10^{14} molecule cm^{-3}, RH= 30 % and Light intensity (I) = 30 mW cm^{-2}. Theoretical sulfate concentration of TiO_2 (50 wt. %)+$CaCO_3$ (50 wt. %) mixtures in each system was obtained from a simple linear superposition of the IC results of individual components and enhancement factors for sulfate ions in two systems could be thus estimated.

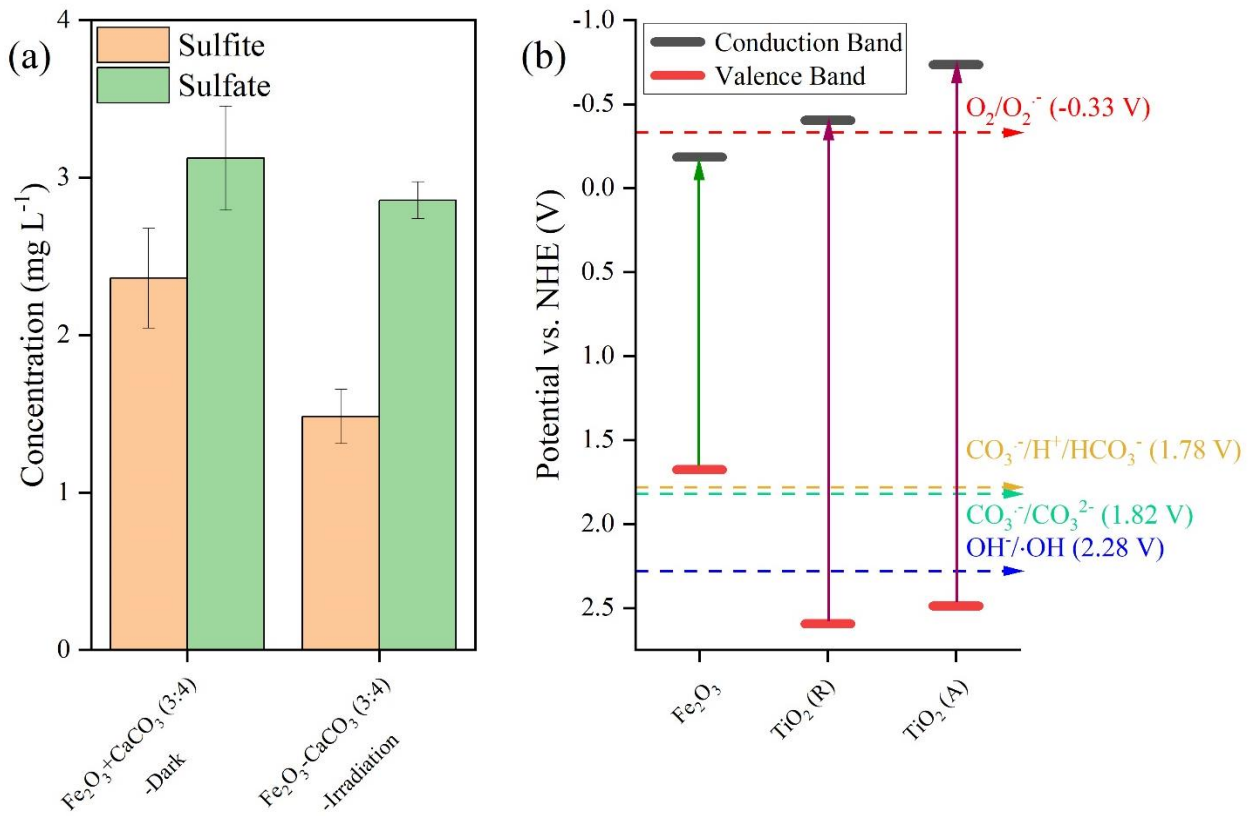

Fig. S9. (**a**) Determination of sulfite and sulfate concentration after exposure to air flow under irradiation in Fe_2O_3+$CaCO_3$ particles for 20 min. (**b**) Band positions of typical active mineral dust components (at pH = 7 in aqueous media), with highlights on the oxidation capability and generation of reactive oxygen species. Reaction conditions: RH = 30 %, Light intensity (I) = 30 mW cm^{-2}, Total flow rate = 52.5 mL min^{-1}.

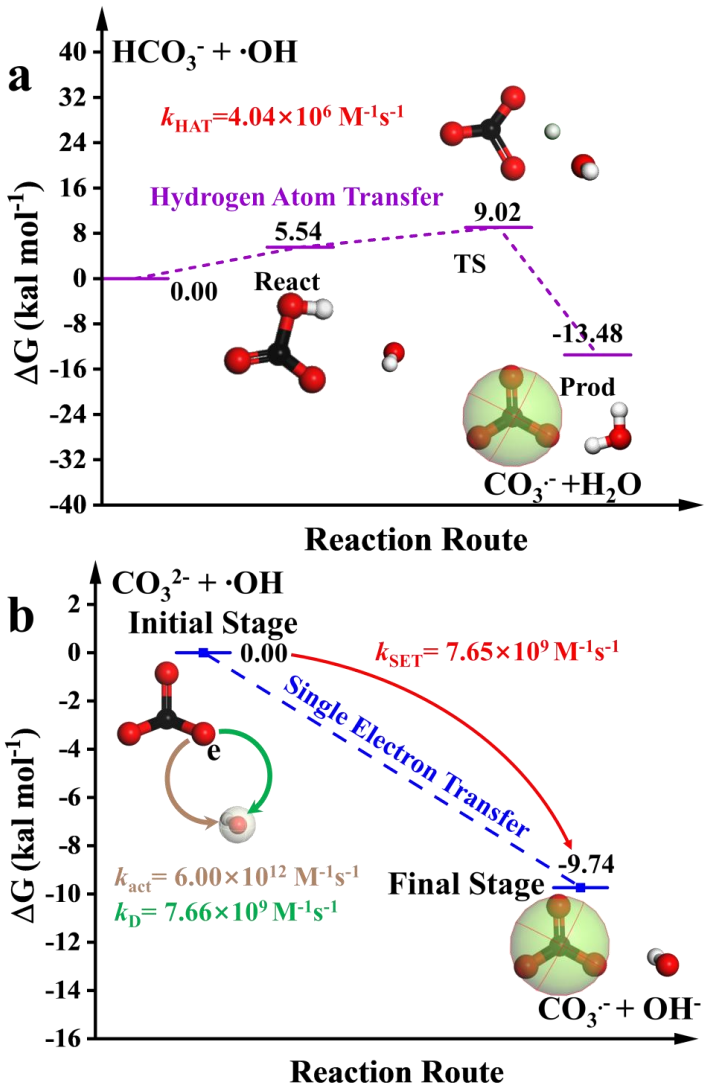

Fig. S10. DFT calculations of two reaction routes for producing carbonate radicals. (**a**) Reaction energy profiles (kcal mol^{-1}) of the HAT reaction through ·OH with HCO_3^- at the CCSD(T)-F12/cc-PVDZ-F12//M06-2X/6-311++G (3df, 3pd) level. The white, black, and red spheres represent H, C, and O atoms, respectively. (**b**) Reaction pathway of the hydroxyl radical (·OH) and CO_3^{2-} through the SET process at the CCSD(T)-F12/cc-PVDZ-F12//M06-2X/6-311++G (3df, 3pd) level, and ΔG^0_{SET} is the difference of Gibbs free energy between reactants and products.

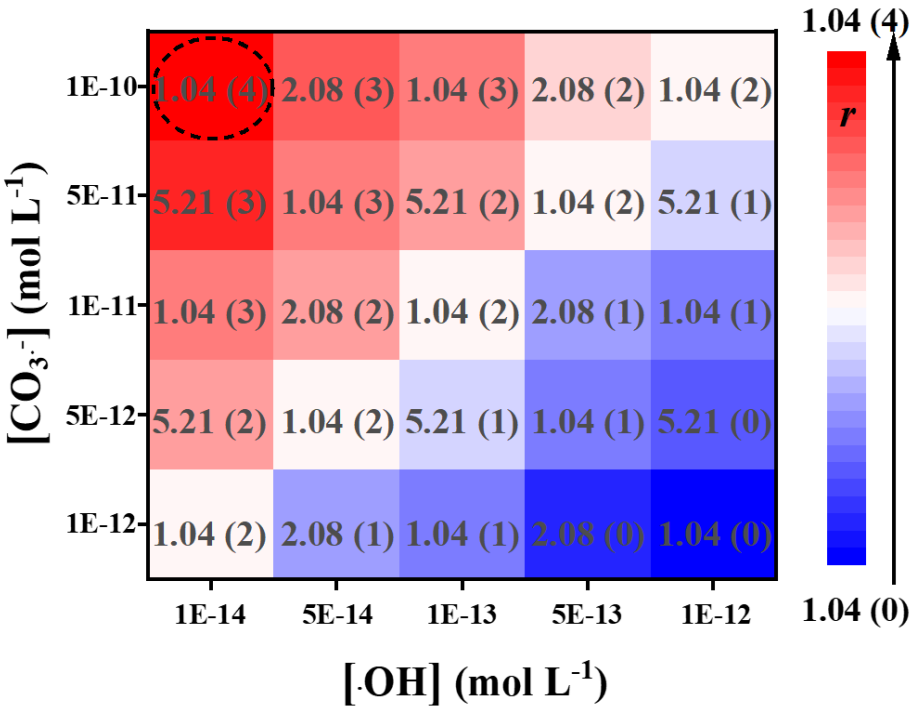

Fig. S11. The ratio of the two reaction rates *r* versus the concentration of $CO_3^{\cdot-}$ and ·OH. Numbers in parentheses referred to powers of ten.

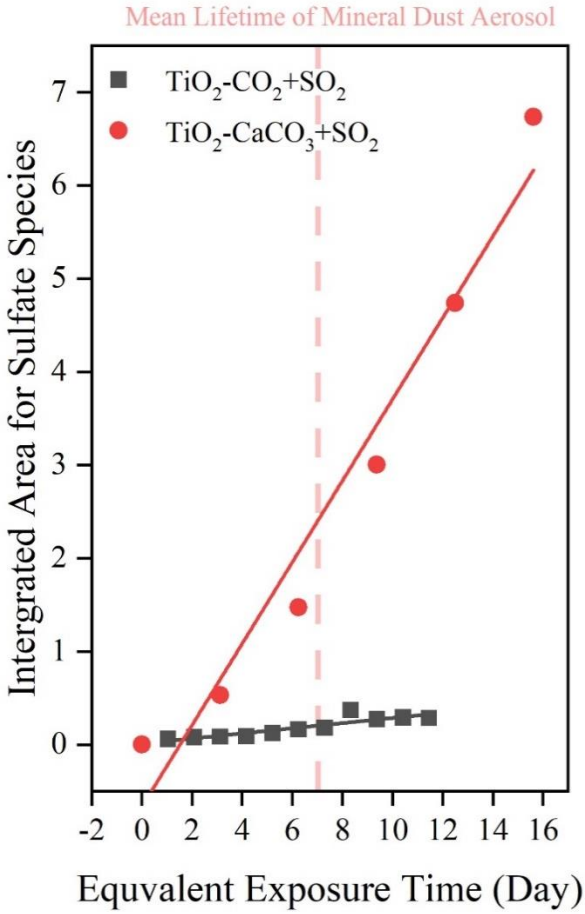

Fig. S12. *In situ* DRIFTS of S(IV) and S(VI) species on TiO_2 and TiO_2 (50 wt. %) + $CaCO_3$ (50 wt. %) upon irradiation as function of equivalent exposure time. Reaction conditions: RH = 30 %, Light intensity (I) = 30 mW cm^{-2}, Total flow rate = 52.5 mL min^{-1}, and CO_2 = 400 ppm.

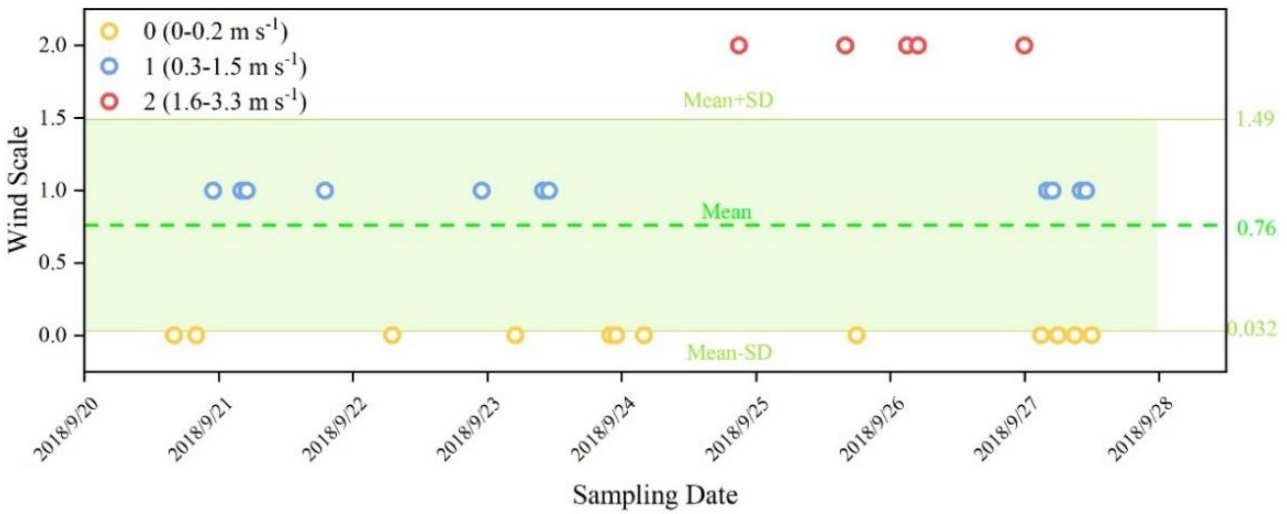

Fig. S13. Daily variations of wind scales from 20 September to 28 September in 2018, Yangpu Sipiao Station, Shanghai.

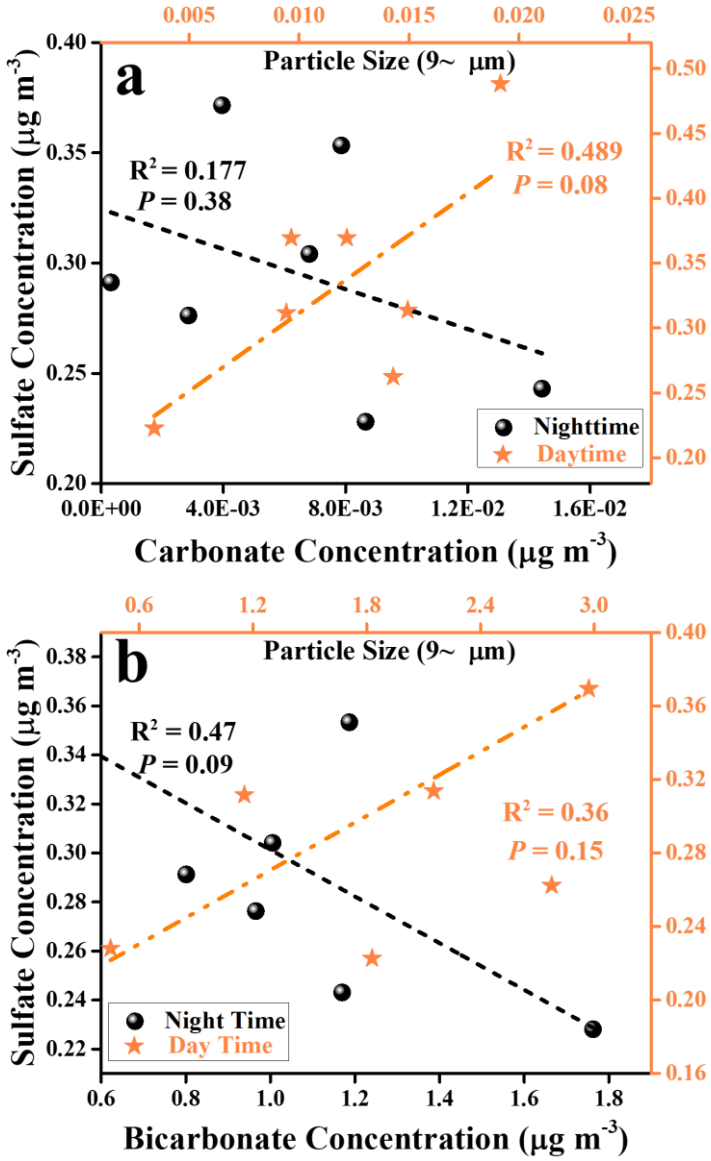

Fig. S14. Field observation for the relationship between carbonate and sulfate ions during daytime and nighttime. Linear relationship analyses for measured sulfate ions and estimated carbonate ions (**a**) and measured sulfate ions and estimated bicarbonate ions (**b**) during the daytime and nighttime hours.

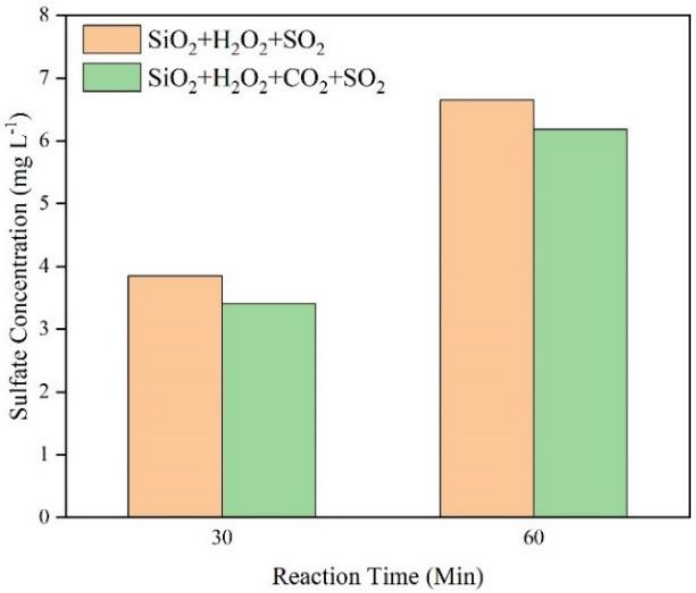

Fig. S15. Sulfate concentration quantified by IC on mineral dust particles after exposure to gaseous SO_2 under irradiation for 30 min in presence of H_2O_2 gas flow. Reaction conditions: Total flow rate = 52.5 mL min^{-1}, SO_2 = 2.21×10^{14} molecules cm^{-3} and CO_2 = 9.83×10^{15} molecules cm^{-3}. To produce gaseous H_2O_2 flow, an airflow was humidified in a bubbler loaded with 100 mM H_2O_2. The detailed protocol is similar to the one we applied for sulfate production over TiO_2 particles (Supplementary Text 1). We performed two sets of experiments with a duration time of 30 min and 60 min, respectively.

Reference

Ali SZ, Kanao F, Takehiro M, Joichi S: Quantitative Estimation of Adsorbed Water Layer on Austenitic Stainless Steel. Tribology Online, 10,314-319, https://doi.org/10.2474/trol.10.314, 2015.

Alivisatos AP: Semiconductor clusters, nanocrystals, and quantum dots. Science, 271,933-937, https://doi.org/10.1126/science.271.5251.933, 1996.

Balachandran U, Eror NG: Raman-Spectra Of Titanium-Dioxide. J. Solid State Chem., 42,276-282, https://doi.org/10.1016/0022-4596(82)90006-8, 1982.

Buchalska M, Kobielusz M, Matuszek A, Pacia M, Wojtyla S, Macyk W: On Oxygen Activation at Rutile- and Anatase-TiO_2. Acs. Catal., 5,7424-7431, https://doi.org/10.1021/acscatal.5b01562, 2015.

Chavadej S, Phuaphromyod P, Gulari E, Rangsunvigit P, Sreethawong T: Photocatalytic degradation of 2-propanol by using Pt/TiO_2 prepared by microemulsion technique. Chem. Eng. J., 137,489-495, https://doi.org/10.1016/j.cej.2007.05.001, 2008.

Chen ZL, Tian ZB, Zhang J, Li F, Du SM, Cui W, et al.: Deep-red-emitting $Ca_2ScSbO_6:Mn^{4+}$ phosphors with a double perovskite structure: Synthesis, characterization and potential in plant growth lighting. J. Am. Ceram. Soc., 105,2094-2104, https://doi.org/10.1111/jace.18221, 2022.

Chrzan K: Conductivity of Aqueous Dust Solutions. Ieee. T. Dielect. El. In., 22,241-244, https://doi.org/10.1109/Tei.1987.298984, 1987.

Crowley JN, Ammann M, Cox RA, Hynes RG, Jenkin ME, Mellouki A, et al.: Evaluated kinetic and photochemical data for atmospheric chemistry: Volume V - heterogeneous reactions on solid substrates. Atmos. Chem. Phys., 10,9059-9223, https://doi.org/10.5194/acp-10-9059-2010, 2010.

Di Fonzo F, Casari CS, Russo V, Brunella MF, Li Bassi A, Bottani CE: Hierarchically organized nanostructured TiO_2 for photocatalysis applications. Nanotechnology, 20,015604, https://doi.org/10.1088/0957-4484/20/1/015604, 2009.

Du C, Kong L, Zhanzakova A, Tong S, Yang X, Wang L, et al.: Impact of adsorbed nitrate on the heterogeneous conversion of SO_2 on α-Fe_2O_3 in the absence and presence of simulated solar irradiation. Sci.Total. Environ., 649,1393, https://doi.org/10.1016/j.scitotenv.2018.08.295, 2019.

Elm J, Bilde M, Mikkelsen KV: Assessment of Density Functional Theory in Predicting Structures and Free Energies of Reaction of Atmospheric Prenucleation Clusters. J. Chem. Theory. Comput., 8,2071-2077, https://doi.org/10.1021/ct300192p, 2012.

Elm J, Jorgensen S, Bilde M, Mikkelsen KV: Ambient reaction kinetics of atmospheric oxygenated organics with the OH radical: a computational methodology study. Phys. Chem. Chem. Phys., 15,9636-9645, https://doi.org/10.1039/c3cp50192b, 2013.

Evans MG, Polanyi M: Some applications of the transition state method to the calculation of reaction velocities, especially in solution., T. Faraday Soc., 31,0875-0893, https://doi.org/10.1039/Tf9353100875, 1935.

Eyring H: The activated complex in chemical reactions. J. Chem. Phys., 3,107-115, https://doi.org/10.1063/1.1749604, 1935.

Fang X, Liu Y, Kejian, Tao W, Yue D, Yiqing F, et al.: Atmospheric Nitrate Formation through Oxidation by carbonate radical. ACS Earth Space Chem., 5,1801–1811, https://doi.org/10.1021/acsearthspacechem.1c00169, 2021.

Gailhanou H, Blanc P, Rogez J, Mikaelian G, Kawaji H, Olives J, et al.: Thermodynamic properties of illite, smectite and beidellite by calorimetric methods: Enthalpies of formation, heat capacities, entropies and Gibbs free energies of formation. Geochim. Cosmochim. Ac., 89,279-301, https://doi.org/10.1016/j.gca.2012.04.048, 2012.

Gao J, Meng YQ, Benton A, He J, Jacobsohn LG, Tong JH, et al.: Insights into the Proton Transport Mechanism in TiO_2 Simple Oxides by In Situ Raman Spectroscopy. ACS Appl. Mater. Inter., 12,38012-38018, https://doi.org/10.1021/acsami.0c08120, 2020.

Goodman AL, Bernard ET, Grassian VH: Spectroscopic study of nitric acid and water adsorption on oxide particles: Enhanced nitric acid uptake kinetics in the presence of adsorbed water. J. Phys. Chem. A, 105,6443-6457, https://doi.org/10.1021/jp0037221, 2001.

Iuga C, Campero A, Vivier-Bunge A: Antioxidant vs. prooxidant action of phenothiazine in a biological environment in the presence of hydroxyl and hydroperoxyl radicals: a quantum chemistry study. Rsc Adv., 5,14678-14689, https://doi.org/10.1039/c4ra14918a, 2015.

Ji YM, Wang HH, Li GY, An TC: Theoretical investigation on the role of mineral dust aerosol in atmospheric reaction: A case of the heterogeneous reaction of formaldehyde with NO2 onto SiO2 dust surface. Atmos. Environ., 103,207-214, https://doi.org/10.1016/j.atmosenv.2014.12.044, 2015.

Jiang HT, Liu YC, Xie Y, Liu J, Chen TZ, Ma QX, et al.: Oxidation Potential Reduction of Carbon Nanomaterials during Atmospheric-Relevant Aging: Role of Surface Coating. Environ. Sci. Technol., 53,10454-10461, https://doi.org/10.1021/acs.est.9b02062, 2019.

Johnson ER, Sciegienka J, Carlos-Cuellar S, Grassian VH: Heterogeneous uptake of gaseous nitric acid on dolomite ($CaMg(CO_3)_{(2)}$) and calcite ($CaCO_3$) particles: A knudsen cell study using multiple, single, and fractional particle layers. J. Phys. Chem. A, 109,6901-6911, https://doi.org/10.1021/jp0516285, 2005.

Johnson SM, Pask JA, Moya JS: Influence of Impurities on High-Temperature Reactions of Kaolinite. J. Am. Ceram. Soc., 65,31-35, https://doi.org/10.1111/j.1151-2916.1982.tb09918.x, 1982.
Joshi N, Romanias MN, Riffault V, Thevenet F: Investigating water adsorption onto natural mineral dust particles: Linking DRIFTS experiments and BET theory. Aeolian Res., 27,35-45, https://doi.org/10.1016/j.aeolia.2017.06.001, 2017.
Kansal SK, Singh M, Sud D: Studies on TiO_2/ZnO photocatalysed degradation of lignin. J. Hazard Mater., 153,412-417, https://doi.org/10.1016/j.jhazmat.2007.08.091, 2008.
Kimball FCCaGE: Diffusion-controlled reaction rates. J. Colloid Sci., 4,425-437, https://doi.org/10.1016/0095-8522(49)90023-9, 1949.
Knizia G, Adler TB, Werner HJ: Simplified CCSD(T)-F12 methods: Theory and benchmarks. J. Chem. Phys., 130,054104, https://doi.org/10.1063/1.3054300, 2009.
Lane JR, Kjaergaard HG: Explicitly correlated intermolecular distances and interaction energies of hydrogen bonded complexes. J. Chem. Phys., 131,034307, https://doi.org/10.1063/1.3159672, 2009.
Li HJ, Zhu T, Zhao DF, Zhang ZF, Chen ZM: Kinetics and mechanisms of heterogeneous reaction of NO_2 on $CaCO_3$ surfaces under dry and wet conditions. Atmos. Chem. Phys., 10,463-474, https://doi.org/10.5194/acp-10-463-2010, 2010.
Li KJ, Kong LD, Zhanzakova A, Tong SY, Shen JD, Wang T, et al.: Heterogeneous conversion of SO_2 on nano alpha-Fe_2O_3: the effects of morphology, light illumination and relative humidity. Environ. Sci. Nano., 6,1838-1851, https://doi.org/10.1039/c9en00097f, 2019.
Liu TY, Abbatt JPD: Oxidation of sulfur dioxide by nitrogen dioxide accelerated at the interface of deliquesced aerosol particles. Nat. Chem., 13,1173-+, https://doi.org/10.1038/s41557-021-00777-0, 2021.
Liu TY, Clegg SL, Abbatt JPD: Fast oxidation of sulfur dioxide by hydrogen peroxide in deliquesced aerosol particles. Proc. Natl. Acad. Sci. USA, 117,1354-1359, https://doi.org/10.1073/pnas.1916401117, 2020.
Luo S, Wei ZS, Dionysiou DD, Spinney R, Hu WP, Chai LY, et al.: Mechanistic insight into reactivity of sulfate radical with aromatic contaminants through single-electron transfer pathway. Chem. Eng. J., 327,1056-1065, https://doi.org/10.1016/j.cej.2017.06.179, 2017.
M. J. Frisch GWT, H. B. Schlegel, G. E. Scuseria, M. A. Robb, J. R. Cheeseman, G. Scalmani, V. Barone, B. Mennucci, G. A. Petersson, H. Nakatsuji, M. Caricato, X. Li, H. P. Hratchian, A. F. Izmaylov, J. Bloino, G. Zheng, J. L. Sonnenberg, M. Hada, K. Ehara, M Toyota, R. Fukuda, J. Hasegawa, M. Ishida, T. Nakajima, Y. Honda, O. Kitao, H. Nakai, T. Vreven, J. A. Montgomery, J. E. Peralta, F. Ogliaro, M. Bearpark, J. J. Heyd, E. Brothers, K. N. Kudin, V. N. Staroverov, R. Kobayashi, J. Normand, K. Raghavachari, A. Rendell, J. C. Burant, S. S. Iyengar, J. Tomasi, M. Cossi, N. Rega, J. M. Millam, M. Klene, J. E. Knox, J. B. Cross, V. Bakken, C. Adamo, J. Jaramillo, R. Gomperts, R. E. Stratmann, O. Yazyev, A. J. Austin, R. Cammi, C. Pomelli, J. W. Ochterski, R. L. Martin, K. Morokuma, V. G. Zakrzewski, G. A. Voth, P. Salvador, J. J. Dannenberg, S. Dapprich, A. D. Daniels, O. Farkas, J. B. Foresman, J. V. Ortiz, J. Cioslowski and D. J. Fox. Gaussian 09. Wallingford CT: Gaussian Inc., 2009.
Marcus RA: Electron transfer reactions in chemistry Theory and experiment. J. Electroanal. Chem., 438,251-259, https://doi.org/10.1016/S0022-0728(97)00091-0, 1997.
Mardirossian N, Head-Gordon M: How Accurate Are the Minnesota Density Functionals for Noncovalent Interactions, Isomerization Energies, Thermochemistry, and Barrier Heights Involving Molecules Composed of Main-Group Elements?, J. Chem. Theory. Comput., 12,4303-4325, https://doi.org/10.1021/acs.jctc.6b00637, 2016.
Marenich AV, Cramer CJ, Truhlar DG: Performance of SM6, SM8, and SMD on the SAMPL1 Test Set for the Prediction of Small-Molecule Solvation Free Energies. J. Phys. Chem. B, 113,4538-4543, https://doi.org/10.1021/jp809094y, 2009.
Mogili PK, Kleiber PD, Young MA, Grassian VH: Heterogeneous uptake of ozone on reactive components of mineral dust aerosol: an environmental aerosol reaction chamber study. J. Phys. Chem. A, 110,13799-807, https://doi.org/10.1021/jp063620g, 2006.
Mottley C, Mason RP: Sulfate Anion Free-Radical Formation by the Peroxidation Of (Bi)Sulfite And Its Reaction with Hydroxyl Radical Scavengers. Arch. Biochem. Biophys., 267,681-689, https://doi.org/10.1016/0003-9861(88)90077-X, 1988.
Neese F: The ORCA program system Wires. Comput. Mol. Sci., 2,73-78, https://doi.org/10.1002/wcms.81, 2012.
Nguyen XQ, Broz Z, Uchytil P, Nguyen QT: Methods for the Determination of Transport Parameters of Gases in Membranes. J. Chem. Soc. Faraday T., 88,3553-3560, https://doi.org/10.1039/FT9928803553, 1992.
Pereira AT, Ribeiro AJM, Fernandes PA, Ramos MJ: Benchmarking of density functionals for the kinetics and thermodynamics of the hydrolysis of glycosidic bonds catalyzed by glycosidases. Int. J. Quantum. Chem., 117,e25409, https://doi.org/10.1002/qua.25409, 2017.
Peters SJ, Ewing GE: Water on Salt: An Infrared Study of Adsorbed H_2O on NaCl (100) under Ambient Conditions. J. Phys. Chem. B, 101,10880-10886, https://doi.org/10.1021/jp972810b, 1997.
Peterson KA, Adler TB, Werner HJ: Systematically convergent basis sets for explicitly correlated wavefunctions: The atoms H, He, B-Ne, and Al-Ar. J. Chem. Phys., 128,084102, https://doi.org/10.1063/1.2831537, 2008.

Qin X, Jing LQ, Tian GH, Qu YC, Feng YJ: Enhanced photocatalytic activity for degrading Rhodamine B solution of commercial Degussa P25 TiO_2 and its mechanisms. J. Hazard Mater., 172,1168-1174, https://doi.org/10.1016/j.jhazmat.2009.07.120, 2009.
Raymond C. Physical Chemistry for the Chemical and Biological Sciences. Sausalito,CA: University Science Books, 2000.
Ruiz-Agudo E, Kudlacz K, Putnis CV, Putnis A, Rodriguez-Navarro C: Dissolution and Carbonation of Portlandite [$Ca(OH)_2$] Single Crystals. Environ. Sci. Technol., 47,11342-11349, https://doi.org/10.1021/es402061c, 2013.
Samuni A, Goldstein S, Russo A, Mitchell JB, Krishna MC, Neta P: Kinetics and mechanism of hydroxyl radical and OH-adduct radical reactions with nitroxides and with their hydroxylamines. J. Am. Chem. Soc., 124,8719-8724, https://doi.org/10.1021/ja017587h, 2002.
Shang J, Li J, Zhu T: Heterogeneous reaction of SO_2 on TiO_2 particles. Sci. China Chem.,2637–2643, https://doi.org/10.1007/s11426-010-4160-3, 2010.
Smoluchowski MV: Mathematical Theory of the kinetics of the coagulation of colloidal solutions. Zeitschriftfuer Physikalische Chemie. Zeitschriftfuer Physikalische Chemie 92,129-168, 1917.
Su WG, Zhang J, Feng ZC, Chen T, Ying PL, Li C: Surface phases of TiO_2 nanoparticles studied by UV Raman spectroscopy and FT-IR spectroscopy. J. Phys. Chem. C, 112,7710-7716, https://doi.org/10.1021/jp7118422, 2008.
Tang WZ, An H: UV/TiO_2 Photocatalytic Oxidation of Commercial Dyes in Aqueous-Solutions. Chemosphere, 31,4157-4170, https://doi.org/10.1016/0045-6535(95)80015-D, 1995.
Tang Y, Li LL, Wang SS, Cheng QT, Zhang J: Tricomponent coupling biodiesel production catalyzed by surface modified calcium oxide. Environ. Prog. Sustain., 35,257-262, https://doi.org/10.1002/ep.12194, 2016.
Toledano DS, Henrich VE: Kinetics of SO_2 adsorption on photoexcited alpha-Fe_2O_3. Journal of Physical Chemistry B, 105,3872-3877, https://doi.org/10.1021/jp003327v, 2001.
Truhlar DG, Hase WL, Hynes JT: Current Status Of Transition-State Theory. J. Phys. Chem., 87,2664-2682, https://doi.org/10.1021/j150644a044, 1983.
Usher CR, Al-Hosney H, Carlos-Cuellar S, Grassian VH: A laboratory study of the heterogeneous uptake and oxidation of sulfur dioxide on mineral dust particles. J. Geophys. Res., 107,4713, https://doi.org/10.1029/2002jd002051, 2002.
Wang T, Liu YY, Deng Y, Fu HB, Zhang LW, Chen JM: The influence of temperature on the heterogeneous uptake of SO_2 on hematite particles. Sci.Total. Envrion., 644,1493-1502, https://doi.org/10.1016/j.scitotenv.2018.07.046, 2018.
Weaver CEJC, Minerals C: The nature of TiO_2 in kaolinite. Clay Clay Miner., 24,215–218, https://doi.org/10.1346/CCMN.1976.0240501, 1976.
Wigner E: On the Penetration of Potential Energy Barriers in Chemical Reactions. Z. Phys. Chem. Abt. B, 19,203-216, 1932.
Xu H, Ouyang SX, Li P, Kako T, Ye JH: High-Active Anatase TiO_2 Nanosheets Exposed with 95% {100} Facets Toward Efficient H_2 Evolution and CO_2 Photoreduction. ACS Appl. Mater. Inter., 5,1348-1354, https://doi.org/10.1021/am302631b, 2013.
Xu QL, Yu JG, Zhang J, Zhang JF, Liu G: Cubic anatase TiO_2 nanocrystals with enhanced photocatalytic CO_2 reduction activity. Chem. Commun., 51,7950-7953, https://doi.org/10.1039/c5cc01087j, 2015.
Yousaf KE, Peterson KA: Optimized auxiliary basis sets for explicitly correlated methods. J. Chem. Phys., 129,184108, https://doi.org/10.1063/1.3009271, 2008.
Zhao Y, Truhlar DG: The M06 suite of density functionals for main group thermochemistry, thermochemical kinetics, noncovalent interactions, excited states, and transition elements: two new functionals and systematic testing of four M06-class functionals and 12 other functionals. Theor. Chem. Acc., 120,215-241, https://doi.org/10.1007/s00214-007-0401-8, 2008.